

***Herschel* observations of deuterated water towards Sgr B2(M)[★]**

C. Comito¹, P. Schilke^{1,2}, R. Rolfs^{1,2}, D. C. Lis³, A. Belloche¹, E. A. Bergin⁴, T. G. Phillips³, T. A. Bell³, N. R. Crockett⁴, S. Wang⁴, G.A. Blake³, E. Caux^{5,6}, C. Ceccarelli⁷, J. Cernicharo⁸, F. Daniel^{8,9}, M.-L. Dubernet^{10,11}, M. Emprechtinger³, P. Encrenaz⁹, M. Gerin⁹, T. F. Giesen², J. R. Goicoechea⁸, P. F. Goldsmith¹², H. Gupta¹², E. Herbst¹³, C. Joblin^{5,6}, D. Johnstone¹⁴, W. D. Langer¹², W.D. Latter¹⁵, S. D. Lord¹⁵, S. Maret⁷, P. G. Martin¹⁶, G. J. Melnick¹⁷, K. M. Menten¹, P. Morris¹⁵, H. S. P. Müller², J. A. Murphy¹⁸, D. A. Neufeld¹⁹, V. Ossenkopf^{2,20}, J. C. Pearson¹², M. Péroul⁹, R. Plume²¹, S.-L. Qin², S. Schlemmer², J. Stutzki², N. Trappe¹⁸, F. F. S. van der Tak²⁰, C. Vastel^{5,6}, H. W. Yorke¹², S. Yu¹², M. Olberg²², R. Szczerba²³, B. Larsson²⁴, R. Liseau²², R. H. Lin¹², L. A. Samoska¹², and E. Schlecht¹²

(Affiliations are available on page 5 of the online edition)

Received 31 May 2010 / Accepted 26 July 2010

ABSTRACT

Observations of HDO are an important complement for studies of water, because they give strong constraints on the formation processes – grain surfaces versus energetic process in the gas phase, e.g. in shocks. The HIFI observations of multiple transitions of HDO in Sgr B2(M) presented here allow the determination of the HDO abundance throughout the envelope, which has not been possible before with ground-based observations only. The abundance structure has been modeled with the spherical Monte Carlo radiative transfer code RATRAN, which also takes radiative pumping by continuum emission from dust into account. The modeling reveals that the abundance of HDO rises steeply with temperature from a low abundance (2.5×10^{-11}) in the outer envelope at temperatures below 100 K through a medium abundance (1.5×10^{-9}) in the inner envelope/outer core at temperatures between 100 and 200 K, and finally a high abundance (3.5×10^{-9}) at temperatures above 200 K in the hot core.

Key words. ISM: molecules – molecular processes – line: formation

1. Introduction

Water is known to be a fundamental ingredient of the interstellar medium. It is a major coolant of star-forming clouds, but, apart from some high-lying maser transitions, is unobservable from the ground because of the atmospheric absorption. The satellites SWAS and *Odin* (Neufeld et al. 2003; Sandqvist et al. 2006) have observed the ground-state ortho-water line, and ISO has observed highly excited transitions (Goicoechea et al. 2004; Cernicharo et al. 2006; Polehampton et al. 2007), although with low spectral resolution. Water is also an important reservoir of oxygen and therefore a key ingredient in the chemistry of oxygen-bearing molecules. Investigations of the water abundance using many lines covering a wide range of excitation levels with high spectral resolution have been among the main reasons for building the HIFI instrument on board *Herschel* (de Graauw et al. 2010; Pilbratt et al. 2010).

Water can be formed in the gas phase through an ion-molecule channel that is initiated by a reaction of H^+ or H_3^+ with atomic oxygen. Alternatively, water can also be formed through highly endothermic reactions that involve atomic oxygen, which reacts with molecular hydrogen to form OH, which in turn can react with molecular hydrogen to form H_2O . The first process

can work in rather diffuse clouds, where the ionization fraction is high, while the second one is efficient only in shocks, because only there the temperatures are high enough to overcome the high endothermicity. In dense gas, which is neither highly ionized nor very hot, these channels do not work efficiently. There it is assumed that water is formed on grain surfaces, where oxygen can react with atomic hydrogen. These icy grain mantles can be studied through observations of the water stretching bands in ice in the infrared (e.g., Gibb et al. 2000), by which the existence of water ice is a well established observational fact. It is then assumed that this ice mantle is returned to the gas phase either through thermal heating (where water ice mantles are destroyed at about 100 K), or through shock sputtering. The net result is that gas-phase water, irrespective of its formation channel, is often observed in regions where the energetics are such that it is not a priori clear if the water has a gas phase or grain surface origin.

Deuterium fractionation, i.e. the enrichment of the deuterated counterpart of a molecular species much above the cosmic $[D]/[H]$ ratio, is a process that is caused by the zero-point energy difference of the vibrational potential. The deuterated species have a lower zero-point energy because of their larger reduced mass. For H_2O and HDO, the difference in energy is 3.4 kJ/mole or 409 K. That means that deuterium fractionation for H_2O takes place mainly at low temperatures. In other words, the $[HDO]/[H_2O]$ ratio should be *high* if the water in question

[★] *Herschel* is an ESA space observatory with science instruments provided by European-led Principal Investigator consortia and with important participation from NASA.

Table 1. Observed HDO lines used in the modeling.

| | J_K | ν (GHz) | E_l/k (K) | Telescope | Ref. |
|----|-------------------|----------------|----------------|-----------|----------|
| 1 | $3_{1,2}-3_{1,3}$ | 481.8 | 144.5 | HIFI | <i>a</i> |
| 2 | $2_{0,2}-1_{1,1}$ | 490.6 | 42.9 | HIFI | <i>a</i> |
| 3 | $1_{1,0}-1_{0,1}$ | 509.2 | 22.3 | HIFI | <i>a</i> |
| 4 | $2_{2,0}-3_{0,3}$ | 537.8 | 131.4 | HIFI | <i>a</i> |
| 5 | $2_{1,1}-2_{0,2}$ | 599.9 | 66.4 | HIFI | <i>a</i> |
| 6 | $1_{1,0}-1_{1,1}$ | 80.6 | 42.9 | IRAM 30-m | <i>b</i> |
| 7 | $3_{1,2}-2_{2,1}$ | 225.9 | 156.7 | IRAM 30-m | <i>c</i> |
| 8 | $2_{1,1}-2_{1,2}$ | 241.6 | 83.6 | SEST | <i>d</i> |
| 9 | $1_{0,1}-0_{0,0}$ | 464.9 | 0.0 | CSO | <i>e</i> |
| 10 | $1_{1,1}-0_{0,0}$ | 893.6 | 0.0 | CSO | <i>f</i> |

Notes. Rows 1 through 5: summary of all the HDO transitions observed in the HIFI bands 1a and 1b towards Sgr B2(M) (this work). Rows 6 through 9: list of previously observed HDO features that were used to constrain the results of our model (see Sect. 3).

References. (*a*) this work; (*b*) Belloche et al., in prep; (*c*) Jacq et al. (1990); (*d*) Nummelin et al. (1998); (*e*) M. Gerin, priv. comm.; (*f*) Comito et al. (2003).

has been formed at a low temperature, i.e. on cold grains, but *low* if it is a product of either PDR or shock chemistry. Observing the [HDO]/[H₂O] ratio is therefore an important clue to the formation mechanisms of H₂O.

This was the goal of the study by Comito et al. (2003, hereafter C03), who investigated the ground-state HDO line at 893 GHz observed with the Caltech Submillimeter Observatory towards Sgr B2(M) and (N), as well as some published high-excitation HDO lines observed with the IRAM 30-m telescope (Jacq et al. 1990). The HDO observations were compared with those of the o-H₂¹⁸O ground-state line from SWAS (Neufeld et al. 2003), and of higher-energy p-H₂¹⁸O transitions observed with the IRAM 30-m by Gensheimer et al. (1996).

The HDO and H₂¹⁸O ground-state lines, observed in absorption, are formed in the outer envelope, while the high-energy transitions trace the central hot core. Up to now, no observations tracing the inner Sgr B2(M) envelope/outer core were available. Comito et al. (2003) concluded that in the outer layer, H₂O was predominantly shock-produced, while the [HDO]/[H₂O] ratio in the hot core showed, as expected, a grain surface origin. Recent HIFI observations in the framework of the guaranteed time key program *Herschel* observations of EXtra-Ordinary Sources (HEXOS) make it now possible to extend the study of the HDO distribution to the full envelope of Sgr B2(M).

Sgr B2(M) and its neighbor Sgr B2(N) are some of the most massive star-formation sites in our Galaxy. Understanding their history and structure will help understanding the formation of massive Galactic center clusters, such as Arches, and will also have ramifications for even more extreme star-formation processes in starburst galaxies, and even in the early universe.

2. Observations

Full spectral scans of HIFI bands 1a and 1b towards Sgr B2(M) ($\alpha_{J2000} = 17^{\text{h}}47^{\text{m}}20.35^{\text{s}}$ and $\delta_{J2000} = -28^{\circ}23'03.0''$) have been carried out on March 20101 and 2, providing coverage of the frequency range 479 through 637 GHz. The HIFI spectral scans are carried out in dual beam switch (DBS) mode, where the DBS reference beams lie approximately 3' east-west or 6' apart.

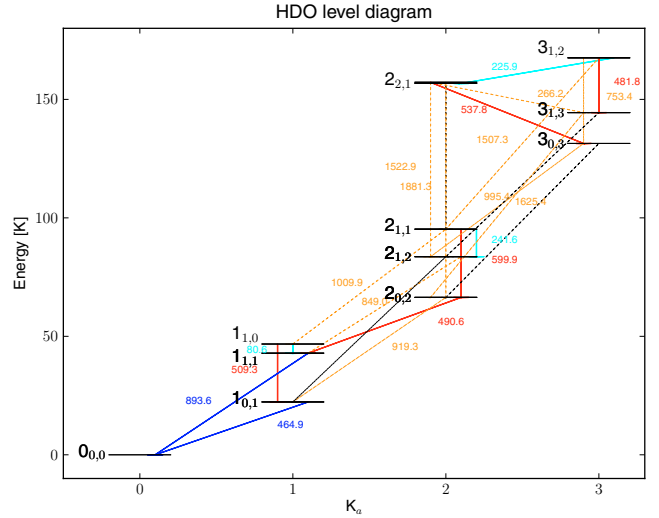


Fig. 1. Level diagram of the HDO lines in the present dataset. The frequency of each transition is indicated in GHz. Transitions are color-coded as follows: in *solid red*, HIFI observations in band 1a and 1b (this work); in *dashed orange*, transitions falling within the overall HIFI range (to be observed within the HEXOS key program); in *dark blue*, submillimeter-wavelength observations (C03; M. Gerin, priv. comm.); in *light blue*, millimeter-wavelength observations from Jacq et al. (1990), Nummelin et al. (1998), and Belloche et al., in prep (cf. Belloche et al. 2008); in *black*, transitions that fall outside of the HIFI range.

The wide band spectrometer (WBS) is used as a back-end, providing a spectral resolution of 1.1 MHz over a 4-GHz-wide Intermediate Frequency (IF) band. A HIFI Spectral Scan consists of a number of double-sideband (DSB) spectra, tuned at different local oscillator (LO) frequencies, where the spacing between LO settings is determined by the “redundancy” selected by the observer (Comito & Schilke 2002). The molecular spectrum of Sgr B2(M) in band 1a and 1b has been scanned with a redundancy of 4 and 8, respectively, which means that every frequency has been observed 4 and 8 times respectively in each sideband. Multiple observations of the same frequency at different LO tunings are necessary to separate the lower-sideband (LSB) from the upper-sideband (USB) spectra.

The data were calibrated through the standard pipeline distributed with version 2.9 of HIPE (Ott 2010), and subsequently exported to CLASS¹ using the HiClass task within HIPE. Deconvolution of the DSB data into single-sideband (SSB) format was performed with CLASS. All the HIFI data presented here, spectral features *and* continuum emission, are deconvolved SSB spectra. Both horizontal (H) and vertical (V) polarizations were obtained. A discrepancy in flux of up to 20% is observed between the two. Because the H data in band 1a and 1b show fewer instrumental artifacts than the V data, we will here show H-polarization spectra only. The intensity scale is main-beam temperature, and is a results of applying a beam efficiency correction of 0.69 for band 1a, and 0.68 for band 1b (Roelfsema et al. 2010) to the deconvolved data.

Table 1 and the level diagram in Fig. 1 summarize the HDO transitions that were observed so far towards Sgr B2(M). Together with those observed with HIFI (top five lines in Table 1, red transitions in Fig. 1), our dataset includes mm-wavelength transitions from the IRAM-30m telescope and from SEST, and

¹ *Continuum and Line Analysis Single-dish Software*, distributed with the GILDAS software, see <http://www.iram.fr/IRAMFR/GILDAS>.

submm-wavelength transitions acquired with the CSO (references are indicated in Table 1). The frequencies were obtained from the JPL Molecular Spectroscopy Catalog (Pickett et al. 1998).

3. Results

The spherical Monte Carlo radiative transfer code RATRAN (Hogerheijde & van der Tak 2000) is employed to compute the intensity of the molecular lines and of the dust continuum. The source model (for a more detailed description see Rolfs et al. 2010) corresponds to a centrally heated source with a density distribution that follows a radial power law with an index of 1.5. The best match between the observed and modeled continuum is achieved through the basic MRN grain size distribution (Ossenkopf & Henning 1994, and references therein), that is, no formation of ice mantles and no coagulation onto the grains is included. The assumed source luminosity is $6.3 \times 10^6 L_{\odot}$. At the inner radius, 1365 AU, the density is $1.5 \times 10^8 \text{ cm}^{-3}$, and the temperature is 1400 K. The temperature is computed in an approximate way from central heating, using the diffusion equation in the inner part and the balance between heating and cooling in the outer part, with an effective temperature of the dust photosphere of 54.5 K. The temperature has a steeper gradient in the inner part (200 K at 0.07 pc; 100 K at 0.14 pc) and decreases to 15 K at the radius of 12.3 pc, where the density is $2.7 \times 10^3 \text{ cm}^{-3}$. From this point on, the temperature and density remain constant, until the outer envelope radius of 22.5 pc is reached (Lis & Goldsmith 1989). This model yields a total H_2 column density of $7 \times 10^{24} \text{ cm}^{-2}$. The HDO collisional rates have been provided by LAMBDA (Leiden Atomic and Collisional Database, Schöier et al. 2005), based on the work of Green (1989).

Figure 2 shows in grey the three HDO emission features detected with HIFI, and also the CSO absorption feature at the bottom. Our best-fit model is overlaid in black. The observed HDO features display a half-power width (HPW) of 14.5 km s^{-1} , and are centered at $v_{\text{LSR}} = 63 \text{ km s}^{-1}$, with the exception of the 894-GHz absorption feature, which is centered at $v_{\text{LSR}} = 64.7 \text{ km s}^{-1}$ (see Fig. 2). This discrepancy is within the uncertainty on the velocity scale that affects HIPE 2. In this work we will use the same velocity parameters ($v_{\text{LSR}} = 63 \text{ km s}^{-1}$, $\Delta v = 14.5 \text{ km s}^{-1}$) for all features in the model.

It has already been demonstrated (C03 and references therein) that a constant HDO abundance across the whole envelope of Sgr B2(M) cannot reproduce the observed intensities of features spanning a relatively wide range of excitation, which means that they arise from different regions within the cloud. It is reasonable to expect a drop in abundance when the gas and dust temperature fall below 100 K, causing the water content of the gas to freeze out onto the dust grains.

With the current model, a simultaneous fit of all the HIFI and CSO transitions (see Fig. 1) is obtained assuming that $[\text{HDO}] = 1.5 \times 10^{-9}$ when $T_{\text{gas}} > 100 \text{ K}$, and $[\text{HDO}] = 1.3 \times 10^{-11}$ when $T_{\text{gas}} < 100 \text{ K}$. However, this two-step abundance model underestimates the intensity of the mm-wavelength features.

Figure 3 shows the normalized populations of the HDO levels of the relevant features in our dataset as calculated by RATRAN. The bulk of the emission for the $J = 3_{1,2}-2_{2,1}$ 226-GHz transition is produced in the inner hot-core region, where $T > 200 \text{ K}$. The other features though arise predominantly in the inner-envelope/outer-core region, with temperatures close to or lower than 100 K. In order to reproduce the intensities of the $3_{1,2}-2_{2,1}$ transition as well, we need to introduce a rise in HDO abundance to about 3.5×10^{-9} , where $T_{\text{gas}} > 200 \text{ K}$.

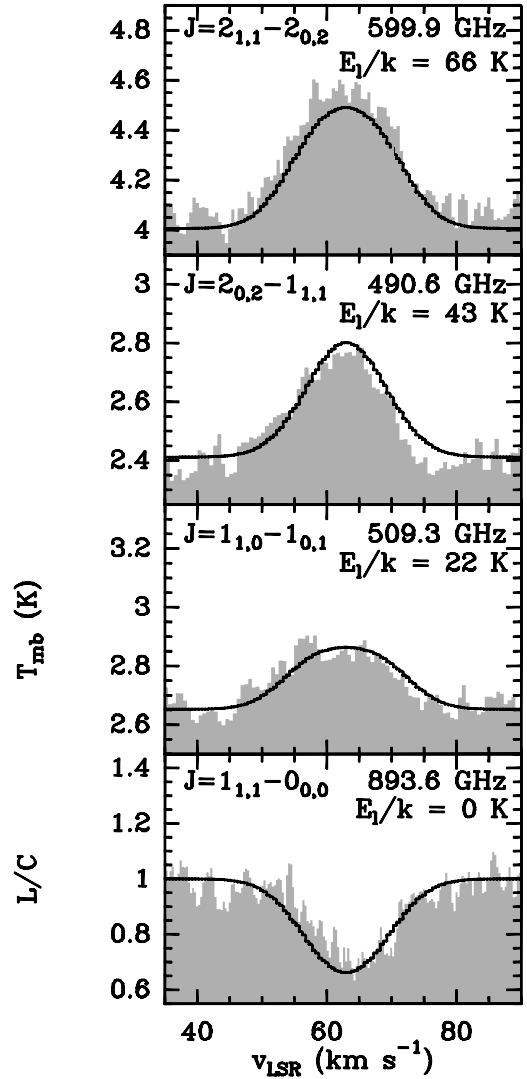


Fig. 2. Grey: the *top three panels* show the HDO emission features detected with HIFI, the *bottom panel* shows the ground-state absorption feature detected with the CSO. Our best-fit model, described in Sect. 3, is overlaid in black. Note that the absorption line is about 2 km s^{-1} off from the center velocity of the emission lines, which is within the uncertainty of the HIFI calibration in HIPE 2.9.

Our model very precisely reproduces 8 out of the 10 transitions in our sample (see Table 2). On the other hand, the $1_{1,0}-1_{1,1}$ and the $2_{1,1}-2_{1,2}$ transitions, at 80.6 and 241.6 GHz respectively, are underestimated by about a factor 3. Although we cannot completely rule out contamination by other species, especially at 3-mm wavelength, where the contribution of unidentified features to the spectrum is about 50% (Belloche et al. 2008), we do not think it realistic that these two features are blended with other, weaker ones to the point of appearing three times stronger than they are. The model's failure to reproduce these lines may be due to the assumption of spherical symmetry, which does not capture all the details of the actual source structure.

4. Discussion

With the *Herschel* lines discussed in this paper, we now possess information about the HDO abundance throughout the envelope (Fig. 3). The physical structure model we employed is based on the structure used by Comito et al. (2003), refined by the study

Table 2. Observed and modeled intensities for all the features in our dataset (see Table 1).

| | J_K | ν (GHz) | $T_{mb,obs}$ (K) | $T_{mb,mod}$ (K) |
|----|------------------------------------|----------------|---------------------|---------------------|
| 1 | 3 _{1,2} -3 _{1,3} | 481.8 | <0.2* | 1×10^{-2} |
| 2 | 2 _{0,2} -1 _{1,1} | 490.6 | 0.4 | 0.4 |
| 3 | 1 _{1,0} -1 _{0,1} | 509.2 | 0.2 | 0.2 |
| 4 | 2 _{2,0} -3 _{0,3} | 537.8 | <0.1* | 2×10^{-4} |
| 5 | 2 _{1,1} -2 _{0,2} | 599.9 | 0.5 | 0.5 |
| 6 | 1 _{1,0} -1 _{1,1} | 80.6 | 0.1 | 4×10^{-2} |
| 7 | 3 _{1,2} -2 _{2,1} | 225.9 | 0.4 | 0.4 |
| 8 | 2 _{1,1} -2 _{1,2} | 241.6 | 5.5** | 1.7** |
| 9 | 1 _{0,1} -0 _{0,0} | 464.9 | <0.7* | 0.6 |
| 10 | 1 _{1,1} -0 _{0,0} | 893.6 | 0.7*** | 0.7 |

Notes. * = upper limit ($3 \times \sigma_{rms}$); ** = integrated area ($K \text{ km s}^{-1}$); *** = line-to-continuum ratio.

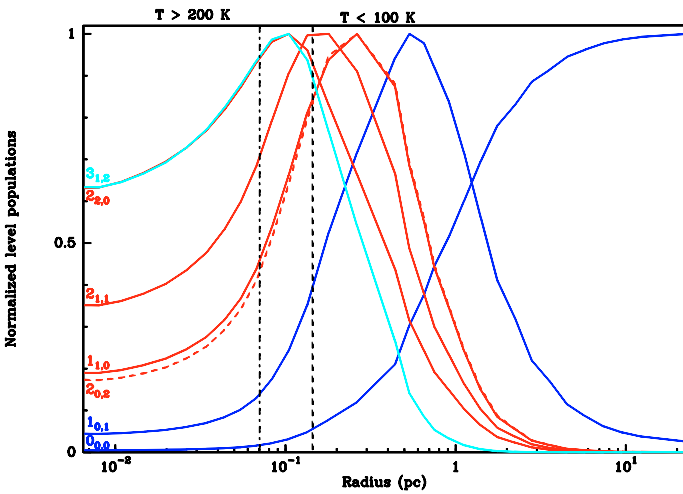


Fig. 3. Normalized fractional level population computed by RATRAN, as a function of the distance from the center of the cloud, for the HDO transitions shown in red, dark blue and light blue in Fig. 1 (the population of level 2_{0,2} is indicated by a dashed red curve, to avoid confusion with level 1_{1,0}). The levels are *upper-energy*, except for the ground-state 893-GHz absorption line, for which the relevant level population is that of the *lower-energy* level.

of Rolfs et al. (2010). We note that we can fit 8 out of 10 lines using this model and a very simple abundance distribution: a low abundance (1.3×10^{-11}) below 100 K, a medium abundance (1.5×10^{-9}) at temperatures between 100 and 200 K, and a high abundance (3.5×10^{-9}) at temperatures above 200 K. This is in contrast to the simpler two-step abundance structure in C03, where no constraints on the HDO abundance from the inner envelope/outer core were available. The exact boundaries of these abundance changes are not well determined, and while evaporation of ice produces a real discontinuity, other processes do not. As mentioned in Sect. 1, no process but ice evaporation can produce HDO in noticeable amounts. In the hot gas phase, this molecule will be formed relative to water with the same abundance of deuterium relative to hydrogen, 1.7×10^{-6} in the Galactic center (Lubowich et al. 2000) which, even if all the oxygen were tied up in water, would correspond to an abundance of only a few times 10^{-10} . This is almost two orders of magnitude

lower than what is observed in the hot gas. A possible explanation for the abundance gradient in gas at $T > 100$ K could be that the ice evaporation is not complete at 100 K, and that the gas-phase HDO abundance gradually increases until a temperature of about 200 K is reached; or that in the inner, denser regions, simply more water (and therefore HDO) has formed on the ice mantles.

To make use of the full information contained in this study, as described in Sect. 1, we need to complement it with the study of H₂O and its isotopologues, and then determine the [HDO]/[H₂O] ratio throughout the envelope. The water modeling will not be as straightforward, because the higher opacities will make the H₂O transitions much more sensitive to deviations from the spherical symmetry. Moreover, water will be produced in outflows (within the core) and shocks (in the outer envelope). However, the comparison will provide necessary clues to the study of the development of the Sgr B2(M) envelope.

Acknowledgements. This paper is dedicated to the memory of Oliver Siebertz (1967-2010).

HIFI has been designed and built by a consortium of institutes and university departments from across Europe, Canada and the United States under the leadership of SRON Netherlands Institute for Space Research, Groningen, The Netherlands and with major contributions from Germany, France and the US. Consortium members are: Canada: CSA, U. Waterloo; France: CESR, LAB, LERMA, IRAM; Germany: KOSMA, MPIfR, MPS; Ireland, NUI Maynooth; Italy: ASI, IFSI-INAF, Osservatorio Astrofisico di Arcetri-INAF; Netherlands: SRON, TUD; Poland: CAMK, CBK; Spain: Observatorio Astronómico Nacional (IGN), Centro de Astrobiología (CSIC-INTA). Sweden: Chalmers University of Technology – MC2, RSS & GARD; Onsala Space Observatory; Swedish National Space Board, Stockholm University – Stockholm Observatory; Switzerland: ETH Zurich, FHNW; USA: Caltech, JPL, NHSC. Support for this work was provided by NASA through an award issued by JPL/Caltech. CSO is supported by the NSF, award AST-0540882.

References

- Belloche, A., Menten, K. M., Comito, C., et al. 2008, *A&A*, 482, 179
 Cernicharo, J., Goicoechea, J. R., Pardo, J. R., & Asensio-Ramos, A. 2006, *ApJ*, 642, 940
 Comito, C., & Schilke, P. 2002, *A&A*, 395, 357
 Comito, C., Schilke, P., Gerin, M., et al. 2003, *A&A*, 402, 635 (C03)
 de Graauw, Th., Helmich, F. P., Phillips, T. G., et al. 2010, *A&A*, 518, L6
 Gensheimer, P. D., Mauersberger, R., & Wilson, T. L. 1996, *A&A*, 314, 281
 Gibb, E. L., Whittet, D. C. B., Schutte, W. A., et al. 2000, *ApJ*, 536, 347
 Goicoechea, J. R., Rodríguez-Fernández, N. J., & Cernicharo, J. 2004, *ApJ*, 600, 214
 Green, S. 1989, *ApJS*, 70, 813
 Hogerheijde, M. R., & van der Tak, F. F. S. 2000, *A&A*, 362, 697
 Jacq, T., Walmsley, C. M., Henkel, C., et al. 1990, *A&A*, 228, 447
 Lis, D. C., & Goldsmith, P. F. 1989, *ApJ*, 337, 704
 Lubowich, D. A., Pasachoff, J. M., Balonek, T. J., et al. 2000, *Nature*, 405, 1025
 Neufeld, D. A., Bergin, E. A., Melnick, G. J., & Goldsmith, P. F. 2003, *ApJ*, 590, 882
 Nummelin, A., Bergman, P., Hjalmarsen, A., et al. 1998, *ApJS*, 117, 427
 Ossenkopf, V., & Henning, T. 1994, *A&A*, 291, 943
 Ott, S. 2010, *Astronomical Data Analysis Software and Systems XIX*, Y. ed. Mizumoto, K.-I. Morita, & M. Ohishi, *ASP Conf. Ser.*, in press
 Pickett, H. M., Poynter, I. R. L., Cohen, E. A., et al. 1998, *Journal of Quantitative Spectroscopy and Radiative Transfer*, 60, 883
 Pilbratt, G. L., Riedinger, J. R., Passvogel, T., et al. 2010, *A&A*, 518, L1
 Polehampton, E. T., Baluteau, J., Swinyard, B. M., et al. 2007, *MNRAS*, 377, 1122
 Roelfsema, P. R., Helmich, F. P., Teyssier, D., et al. 2010, *A&A*, submitted
 Rolfs, R., Schilke, P., Comito, C., et al. 2010, *A&A*, 521, L46
 Sandqvist, A., Bergman, P., Bernath, P., et al. 2006, *J. Phys. Conf. Ser.*, 54, 72
 Schöier, F. L., van der Tak, F. F. S., van Dishoeck, E. F., & Black, J. H. 2005, *A&A*, 432, 369

-
- ¹ Max-Planck-Institut für Radioastronomie, Auf dem Hügel 69, 53121 Bonn, Germany
e-mail: ccomito@mpi.fr.de
- ² I. Physikalisches Institut, Universität zu Köln, Zùlpicher Str. 77, 50937 Köln, Germany
- ³ California Institute of Technology, Cahill Center for Astronomy and Astrophysics 301-17, Pasadena, CA 91125, USA
- ⁴ Department of Astronomy, University of Michigan, 500 Church Street, Ann Arbor, MI 48109, USA
- ⁵ Centre d'étude Spatiale des Rayonnements, Université de Toulouse [UPS], 31062 Toulouse Cedex 9, France
- ⁶ CNRS/INSU, UMR 5187, 9 avenue du Colonel Roche, 31028 Toulouse Cedex 4, France
- ⁷ Laboratoire d'Astrophysique de l'Observatoire de Grenoble, BP 53, 38041 Grenoble, Cedex 9, France
- ⁸ Centro de Astrobiología (CSIC/INTA), Laboratorio de Astrofísica Molecular, Ctra. de Torrejón a Ajalvir, km 4 28850, Torrejón de Ardoz, Madrid, Spain
- ⁹ LERMA, CNRS UMR8112, Observatoire de Paris and École Normale Supérieure, 24 Rue Lhomond, 75231 Paris Cedex 05, France
- ¹⁰ LPMAA, UMR7092, Université Pierre et Marie Curie, Paris, France
- ¹¹ LUTH, UMR8102, Observatoire de Paris, Meudon, France
- ¹² Jet Propulsion Laboratory, Caltech, Pasadena, CA 91109, USA
- ¹³ Departments of Physics, Astronomy and Chemistry, Ohio State University, Columbus, OH 43210, USA
- ¹⁴ National Research Council Canada, Herzberg Institute of Astrophysics, 5071 West Saanich Road, Victoria, BC V9E 2E7, Canada
- ¹⁵ Infrared Processing and Analysis Center, California Institute of Technology, MS 100-22, Pasadena, CA 91125, USA
- ¹⁶ Canadian Institute for Theoretical Astrophysics, University of Toronto, 60 St George St, Toronto, ON M5S 3H8, Canada
- ¹⁷ Harvard-Smithsonian Center for Astrophysics, 60 Garden Street, Cambridge MA 02138, USA
- ¹⁸ National University of Ireland Maynooth, Ireland
- ¹⁹ Department of Physics and Astronomy, Johns Hopkins University, 3400 North Charles Street, Baltimore, MD 21218, USA
- ²⁰ SRON Netherlands Institute for Space Research, PO Box 800, 9700 AV, Groningen, The Netherlands
- ²¹ Department of Physics and Astronomy, University of Calgary, 2500 University Drive NW, Calgary, AB T2N 1N4, Canada
- ²² Chalmers University of Technology, 412 96 Göteborg, Sweden
- ²³ N. Copernicus Astronomical Center, Rabianska 8, 87-100, Torun, Poland
- ²⁴ Department of Astronomy, Stockholm University, 106 91 Stockholm, Sweden